Available online at www.sciencedirect.com

ScienceDirect

journal homepage: www.elsevier.com/locate/he

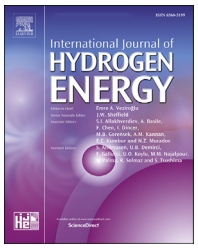

Two-dimensional modeling for physical processes in direct flame fuel cells

Jinyong Kim [a,*], Ankit Tyagi [a], Yongmo Kim [b]

[a] Department of Mechanical & Nuclear Engineering, The Pennsylvania State University, University Park, PA, 16802, USA

[b] Department of Mechanical Engineering, Hanyang University, Seoul, 133-791, Republic of Korea

ARTICLE INFO

Article history:
Received 27 October 2018
Received in revised form
18 December 2018
Accepted 22 December 2018
Available online 18 January 2019

Keywords:
Direct flame fuel cell
SOFC
Multi-dimensional effect
Numerical modeling
SDC

ABSTRACT

Commercial direct flame fuel cells (DFFC) need larger cell surface area for higher power output. In such cases, multi-dimensional effects play significant roles on cell performances. In this work, a two-dimensional numerical model is developed to illustrate physical behaviors associated with the multi-dimensional effects in DFFCs. It is revealed that DFFCs suffer from the negative consequences of non-uniform distributions of temperature, species and voltage in radial direction. Non-uniform distributions of temperature and species results in the decrease of current density at edge regions of DFFCs, owing to lower ionic conductivities and fuel species concentration. And the non-uniform voltage distribution in radial direction causes the decreases of current density at center regions of DFFCs due to the lower over-potential there. Therefore, current density distributions in electrolytes are likely to be M-shaped. The multi-dimensional effects become progressively important with increasing the size of solid oxide fuel cells. Comparing with the DFFC with a SOFC with small cell radius (6.5 mm), a DFFC with a SOFC with large cell radius (33.75 mm) has 25–30% lower maximum power density. We also reveal that cross-over electronic currents in samaria-doped-ceria electrolytes and fuel species starvation due to the secondary oxidation are dominant factors on the cell performance loss at high cell temperatures (~1000 K).

Introduction

A direct flame fuel cell (DFFC) is a solid oxide fuel cell (SOFC) that directly utilizes intermediate species (H_2, CO) generated from a fuel-rich hydrocarbon flame [1–8]. To address the working principle of a DFFC system, a schematic configuration is displayed in Fig. 1a. As illustrated in the figure, fuel-rich premixed flames [1,4,6,7] or diffusion flames [5], heat up the DFFC to the temperature required for sufficient electrochemical reactions (500–700 °C), and produce H_2 and CO via incomplete combustion. Major advantages of DFFCs include rapid start-up [2], chamber-free fuel cell system and a wide range of fuel selection [1,4,5]. Owing to these advantages, DFFCs have been getting more attention, especially for mobile [1,7–9] and combined heat/power applications [2,3,6,10,11].

The development of DFFCs, however, is still at early stages with many problems to overcome. One of the major drawbacks of DFFCs is their low power output due to high activation and concentration losses. For example, experimental

* Corresponding author.
E-mail address: jxk621@psu.edu (J. Kim).
https://doi.org/10.1016/j.ijhydene.2018.12.169

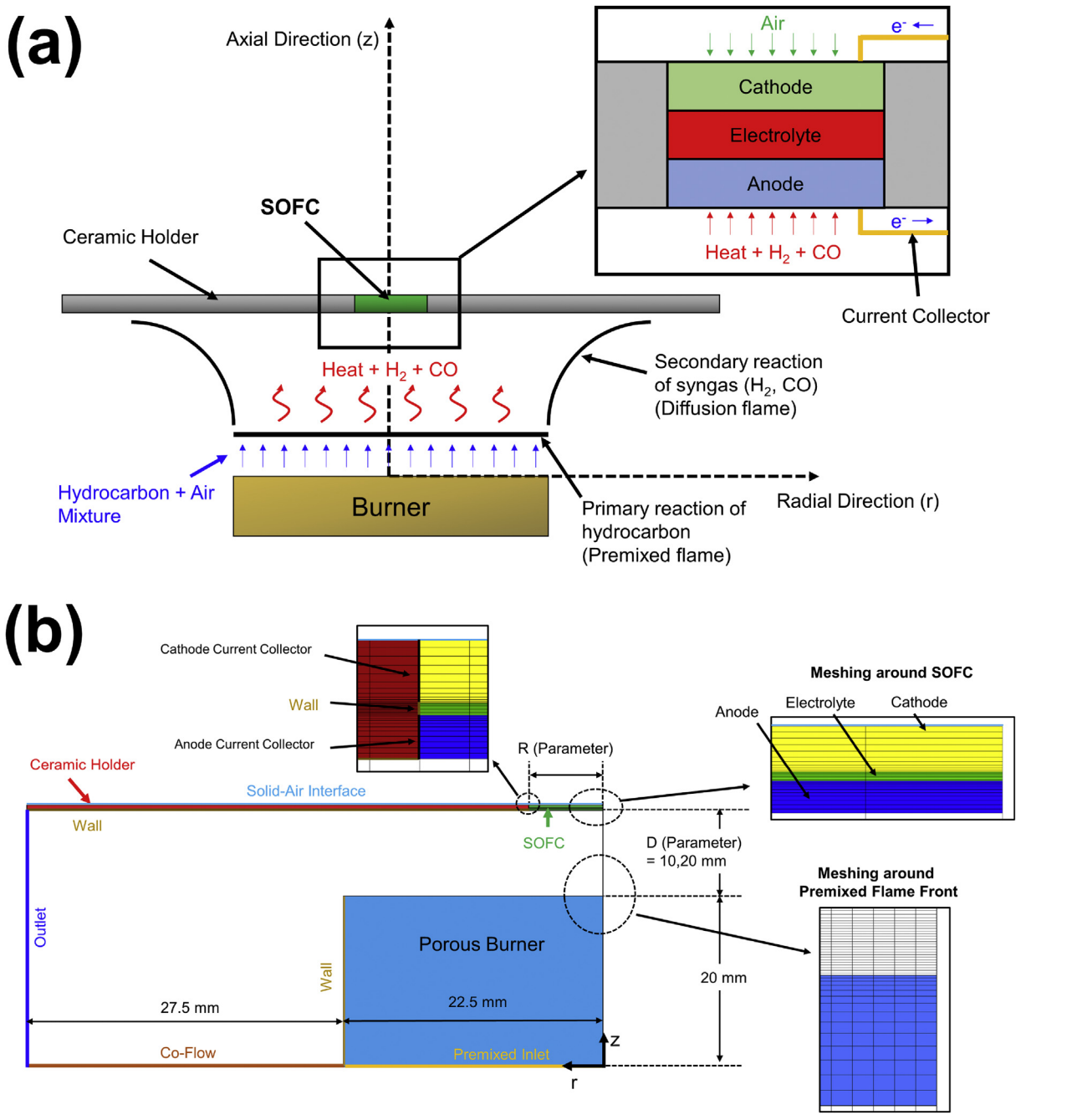

Fig. 1 – (Color Online) (a) Schematic illustration of direct flame fuel cell operated on flat premixed flame (Re-drawn from Kronemayer et al. [7]) (b) Computational geometry and numerical mesh.

studies [1,2,4,7,9–13] have shown that DFFCs have much lower limiting current densities (0.1–1.0 A cm^{-2}), compared to limiting current densities of SOFCs (4–8 A cm^{-2}) using state-of-art materials [14–18]. This is attributed from the small molar concentrations (mole fraction = 1–10%) of electro-chemically active species in the partially-oxidized exhaust gas of fuel-rich premixed flame [7,8]. In order to overcome this issue, understanding the physical behavior occurring between flame and SOFC is crucial.

Another urgent task for the commercialization of DFFCs is to maximize electro-chemically active surface area to increase power outputs [9]. However, most of SOFCs used in prior experimental works for DFFCs are not large enough (surface areas ~ 1 cm^{-2}) to produce enough power for mobile applications. To name a few, the diameter of the fuel cell used in the experiment of Kronemayer et al. [7] is 13 mm, which is considerably smaller than the diameter of burner (45 mm). Also, the cell surface used in the experiment by Tucker et al. [19] is as small as 1 cm^2. At a power density of 0.1 W cm^{-2}, the power output from the SOFC with an active surface area of 1 cm^2 would yield a 0.1 W power output. For mobile applications, DFFCs may need to produce power outputs larger than

10 W to successfully operate electrical devices, such as cell phone chargers (~10 W). Tucker [9] is the first who pointed out the importance of increasing electrochemically active surface areas for practical DFFC applications, and successfully delivered enough electrical power to cell phone chargers with power output of 2.7 W. Tucker [9] used a 5-cell-stack configuration with a total cell surface area of 17 cm^2.

Taking these drawbacks into consideration, future commercial DFFCs need to increase the cell surface area together with optimally controlled fuel flow rate, flow-field structure, higher catalytic activities and larger ionic conductivities. In this work, we particularly focus on the effect of cell sizes on key properties of DFFCs, to analyze potential issues for the development of commercial scale DFFCs. With a large cell surface area, it is expected that physical processes in DFFCs could be progressively influenced by multi-dimensional effects in temperature fields and current densities. Thus, it is quite desirable to precisely analyze the multi-dimensional effects in DFFCs with large surface areas. To date, two modeling papers have been reported in the field of DFFCs to elucidate detailed physical phenomena occurring in DFFCs [8,20]. However, the focuses of these paper are far from multi-dimensional effects in DFFCs. Vogler et al. [8] reported a pioneering work on DFFC modeling by presenting one-dimensional model to analyze physical behaviors of DFFCs. Wang et al. [20] presented an axisymmetric two-dimensional model that is applicable for DFFCs with micro-tubular SOFCs.

In this regard, a 2D model is developed in this work to numerically investigate the detailed physical processes and potential multi-dimensional effects encountered in DFFCs. To assess the prediction capability of the present approach, the two-dimensional model is first validated against the experimental measurements of Kronemayer et al. [7]. Then, computations are made for the wide range of cell sizes to discuss the multi-dimensional effects in detail.

Numerical model

Model assumptions

Methane, which is the simplest type of hydrocarbon fuel, is selected as a fuel for premixed flame with air (N_2:O_2 = 79:21) as an oxidizer and two-dimensional computation domains with different cell geometries are selected to investigate axial and radial distributions of key parameters. Current simulation setups are based on the experiment by Kronemayer et al. [7], and more detailed descriptions of computational domains and operating conditions can be found in Section 2.3. Assumptions are made to simplify the problem for clearer elucidations of the underlying physics, as shown below.

- Steady state, laminar flow
- Heat generation due to electro-chemical reactions is ignored, since heat generation in the premixed flame is dominant
- Soot generation is not considered
- Heating due to viscous dissipation is not considered due to small velocities (~0.1 m/s)

Governing equations

Governing physics in DFFCs include gas-phase combustion, electrochemical reaction and charge transport, which can be described in vector form as [21]:

Continuity:

$$\nabla\cdot(\rho\vec{u}) = \dot{S}_{mass} \tag{1}$$

Momentum conservation:

$$\nabla\cdot(\rho\vec{u}\vec{u}) = \nabla\cdot\vec{\tau} - \nabla P + \dot{S}_{mom} \tag{2}$$

Species conservation:

$$\nabla\cdot(\rho\vec{u}Y_i) = \nabla\cdot(\vec{J}_i) + \dot{S}_i \tag{3}$$

Energy conservation:

$$\nabla\cdot(\rho c_p\vec{u}T) = \nabla\cdot\left(k_{eff}\nabla T - \sum_i h_i\vec{J}_i\right) + \dot{S}_T \tag{4}$$

Charge conservation for electron and oxygen ion:

$$0 = \nabla\cdot(\sigma_{eff,char}\nabla\Phi_{char}) + \dot{S}_{\Phi,char} \tag{5}$$

In the following sub-sections, the details of physical parameters, source terms and constitutive relationships used in Eqs. (1)–(5) are addressed.

Combustion in gas-phase and flow model

The major difference between typical SOFCs and DFFCs is the presence of gas-phase combustion. In order to capture detailed flame physics with acceptable accuracy, sufficient number of species (>20) and chemical reactions (>100) are needed to be considered [22]. In this regard, GRI 1.2 mechanism is adopted [23,24], which features 31 chemical species and 175 chemical reactions. In order to accelerate computation speed, the in-situ adaptive tabulation (ISAT) [25] method is used with the error tolerance of 3×10^{-5} and a table size of 500 MB.

The diffusion of gaseous species is described by the dilute approximation, rather than the full multi-component diffusion, since it yields a good approximation for air-methane combustion [26] and computationally more efficient [26]. Species diffusivities are described by using a constant non-unity Lewis number approximation method to capture detailed flame structures with excellent accuracy [27]. Due to high mole fraction of nitrogen (~0.79), the mixture-averaged diffusivity of species-k [28] is approximated to the binary diffusion coefficient of species-k to nitrogen as:

$$D_{k,m} = \frac{1-Y_k}{\sum_{k\neq i}X_k/D_{i-k}} \approx D_{k-N_2} \tag{6}$$

We assume that the Lewis number for oxygen is 1 based on literature [27,29], hence, the Lewis number for each species is approximated as:

$$Le_k = \frac{D_{O_2-N_2}}{D_{k-N_2}} \tag{7}$$

where the binary diffusion coefficient of species-k to nitrogen is evaluated by the Chapman-Enskog kinetic theory [28] at 2000K [22]. The Lewis number of each species evaluated

with the current method can be found in the Supplementary material. Once the Lewis number of each species is obtained, the mixture-averaged diffusivity of species-k can be described by:

$$D_{k,m} = \frac{\alpha}{Le_k} \tag{8}$$

The result from the constant non-unity Lewis number-based binary species diffusion method is compared to the result from the full multi-component diffusion method in the Supplementary material I and species Lewis numbers can be found in the Supplementary material II.

The species diffusion in porous electrodes is very important, since it is the main mechanism to transport fuel species to catalyst layers for electrochemical reactions in SOFCs. In this work, the effective diffusivity of each species is described by the Bosanquet treatment [30] as:

$$D_{k,eff} = \frac{\varepsilon}{\tau} D_{k,m} \tag{9}$$

where ε is a porosity and τ is a tortuosity. And the pressure loss due to the viscous friction between porous structures and the gas flow is described by the Darcy's law as:

$$\dot{S}_{mom} = -\frac{\mu}{K}\vec{u} \tag{10}$$

Permeabilities of porous electrodes and porous burner was not reported in the experimental paper by Kronemayer et al. [7]. However, considering that the range of pore sizes and porosities of commercial porous burners are within 0.5–2 mm and 0.5–0.7, respectively, the range of permeability of porous burners are on the magnitude of 10^{-8} m^2 according to the Kozeny-Carman relationship. In this work, 10^{-8} m^2 is assumed for the permeability of the porous burner.

The radiative heat transfer also plays an important role on cell performances. For example, a large amount of heat is dissipated from SOFCs to environment by radiation due to high surface temperatures. In the current work, the P1 model [31,32] and the weighted-sum-of-gray-gases model (WSGGM) [33,34] are adapted to describe the radiative heat transfer from the surfaces as well as gas-phase combustion.

Electro-chemical reactions and charge transport

Electrochemical reactions of fuel species, such as hydrogen (H_2) and carbon monoxide (CO) from incomplete gas-phase combustions, are the driving forces of DFFCs. In this work, electrochemical reactions are described by the Butler-Volmer equation as:

$$j_i = j_{0,i}\left[\exp\left(\frac{\alpha_i n_i F \eta_i}{RT}\right) - \exp\left(-\frac{(1-\alpha_i) n_i F \eta_i}{RT}\right)\right] \tag{11}$$

where $j_{0,i}$ is a volumetric exchange current density of species-i, which is strongly affected by temperature and species concentration. The expressions of volumetric exchange current densities for H_2 and CO (**Eq.** (12 and 13)) are taken from Bao et al. [14], and the expression for O_2 (**Eq.** (14)) is taken from Vogler et al. [8].

$$j_i = j_{0,H_2,ref}\left(\frac{P_{H_2}}{P_{H_2,ref}}\right)^{0.734}\left[\exp\left(-\frac{E_{act,H_2,ex}}{RT}\right)\right] \tag{12}$$

$$j_i = j_{0,CO,ref}\left(\frac{P_{CO}}{P_{CO,ref}}\right)^{1.65}\left[\exp\left(-\frac{E_{act,CO,ex}}{RT}\right)\right] \tag{13}$$

$$j_i = j_{0,O_2,ref}\left(\frac{P_{O_2}}{P_{O_2,ref}}\right)^{1/4}\left(1+\frac{P_{O_2}}{P_{O_2,ref}}\right)^{-1/2}\left[\exp\left(-\frac{E_{act,O_2,ex}}{RT}\right)\right] \tag{14}$$

According to the Butler-Volmer equation, electrochemical reactions are driven by the over-potential (η), which is defined as $\eta = \phi_s - \phi_e - E_0$, where E_0 is an equilibrium potential. Expressions for equilibrium potentials of H_2 and CO oxidation can be found in Ref. [35], and therefore are not repeated here. Since both H_2 and CO can be oxidized via electro-chemical reaction, the total volumetric current density due to fuel oxidation at anode catalyst layers is $j = j_{H_2} + j_{CO}$, and the source term of each species due to electro-chemical reaction is $\dot{S}_i = j_i/(n_i F)$. Therefore, the mass source term due to electro-chemical reaction in electrodes is $\dot{S}_{mass} = \sum_i MW_i j_i/(n_i F)$.

Once electrons and oxygen ions are generated via electro-chemical reaction, they are driven by electric forces due to potential gradient. This process causes Ohmic loss in electrolytes and electrodes. Ionic conductivity of samaria-doped-ceria (SDC), which is selected as a material for electrolytes, can be expressed in an Arrhenius form as:

$$\sigma_{ion} = \frac{A_{ion}}{T}\exp\left(-\frac{E_{act,ion}}{RT}\right) \tag{15}$$

In porous electrodes, the effective ionic conductivity is further decreased due to lower volume fractions of SDCs and tortuous porous structures [35]. To account for this effect, the effective ionic conductivity in electrodes is described by the Bosanquet treatment [30] in the current model as $\sigma_{ion,eff} = \sigma_{ion}\varepsilon_{SDC}/\tau_{SDC}$.

SDC electrolytes act as mixed ion and electron conductors (MIEC), and therefore the effect of cross-over current in SDC electrolytes should be accounted for in numerical models [36–41]. The electronic conductivity of SDC in electrolyte can be expressed as [36–41]:

$$\sigma_{elec,SDC} = \frac{A_{elec}}{T}\exp\left(-\frac{E_{act,elec}}{RT}\right)P_{O_2}^{-0.25} \tag{16}$$

According to Eq. (16), electronic conductivity of SDC is sensitive to local oxygen partial pressure, which ranges from 10^{-25} to 0.21 bar from anode to cathode, respectively [36–41]. Assuming the variations of temperature and ionic conductivity along through-plane direction (x) are negligible, oxygen partial pressure profile along through-plane direction can be described by the 1D analytical model developed by Shen et al. [40] as:

$$\frac{P_{O_2}(x)^{-0.25} - A_0}{P_{O_2}(x_{an|el})^{-0.25} - A_0} = \exp\left(\frac{-F}{RT}\times\frac{\eta_{Ohm}(z - z_{an|el})}{L_{el}}\right) \tag{17}$$

where Ohmic loss inside membrane is defined as $\eta_{Ohm} = \phi_s(z_{an|el}) - \phi_s(z_{el|ca})$. If the oxygen partial pressures at the boundaries are known (atz $= z_{an|el}$, $x_{el|ca}$), the constant A_0 can be expressed as below [39,40]:

$$A_0 = \frac{P_{O_2}(z_{ca|el})^{-0.25} - P_{O_2}(z_{an|el})^{-0.25}\exp(-\eta_{Ohm}F/RT)}{1-\exp(-\eta_{Ohm}F/RT)} \tag{18}$$

Due to significant variations of oxygen partial pressure in SDC (from 10^{-20}bar to 0.21 bar), large number of computational meshes in the thickness direction are required, which increases computational costs. However, for macroscopic simulations, capturing detailed oxygen partial pressure variations in electrolytes is not necessary. Therefore, an effective electronic conductivity is suggested to simplify the electron transport process in SDC electrolytes below, considering that the area-specific resistance (ASR) of the electronic current in electrolytes along the thickness direction can be described as:

$$\frac{1}{ASR_{elec,SDC}} = \frac{L_{electrolyte}}{\sigma_{elec,SDC,eff}} = \int_{z_{an/el}}^{z_{ca/el}} \frac{dz}{\sigma_{elec,SDC}} \tag{19}$$

Assuming negligible temperature variations along the thickness direction, analytic integration of the RHS in Eq. (19) is possible using Eq. (16) and Eq. (17) as:

$$\sigma_{elec,SDC,eff} = \frac{A_{elec}}{T}\exp\left(-\frac{E_{act,elec}}{RT}\right)P_{O_2,eff}^{-0.25} \tag{20}$$

where the effective oxygen partial pressure in SDC electrolytes$P_{O_2,eff}$, is the value that satisfies:

$$\frac{1}{P_{O_2,eff}^{-0.25}} = \int_{x_{an/el}}^{x_{ca/el}} \frac{dx/L}{P_{O_2}^{-0.25}} \tag{21}$$

Analytical derivation and the expression of $P_{O_2,eff}$ can be found in the **Appendix** section. A value of 10^{-20}bar is used for the oxygen partial pressure at the interface between anodes and electrolytes, which is a common under typical SOFC operations [36–40].

Computational geometry, boundary conditions and operating conditions

Detailed computational geometry used in this work is shown in Fig. 1b. Two gas flow inlets are specified: a fuel mixture inlet and a co-flow inlet. A velocity of 0.2 m/s is set at fuel mixture inlet with different mixture compositions depending on various fuel equivalence ratios. At the co-flow inlet, a velocity of 0.2 m/s with the standard mixture composition of air (N_2:O_2 = 79:21) is assumed. In the experimental study by Kronemayer et al. [7], the porous burner is cooled by liquid water. In this regard, we set the temperature of the porous burner at 300 K; the detailed information on the porous burner structure is unknown and beyond the scope of this work.

The properties of the reactant gas flow coming out from the burner are the governing factors on cell performances, and therefore, major emphasis is placed on modeling detailed physics of the reactant gas at anode sides with fine computational meshes (~9000 nodes). Especially, computational meshes at the region around the flame front (within 2 mm from porous burner) are highly refined to capture primary reactions, as shown in Fig. 1b.

The flow above the cathode surface and the ceramic holder is treated relatively simply since major emphasis is placed on the modeling of the reactant flow. At the interface between cathodes and adjacent flow-fields, a mole fraction of oxygen of 0.21 is specified and oxygen consumption mechanism at the cathode is assumed to be purely diffusional due to the low velocity inside porous electrodes.

A heat flux boundary condition is set at the interface between the solid zone (SOFC + ceramic holder) and the adjacent air flow-fields (*lines with sky-blue color in* Fig. 1b), with a functional form of $(h_{eff} + h_{rad})(T - T_\infty)$, where $h_{rad} = \varepsilon\sigma_{SB}(T + T_\infty)(T^2 + T_\infty^2)$. The temperature at the far-field, T_∞, is set to be 300 K. Except for radiative heat transfer, the heat removal from the solid zone is mainly governed by natural convection. The effective heat transfer coefficient for natural convection, h_{eff}, is simply evaluated by the well-known relationship of $Nu = 0.54Ra^{0.25}$ [42], which corresponds to a value of 15 W m^{-2} K^{-1} if the cell temperature is around 900 K. To study the behavior of DFFCs at higher temperatures, another thermal condition, with lower effective heat transfer coefficient and emissivity is considered. This can be realized by adding an insulation over the cathode surface to reduce the heat removal rate [19], which will be discussed in more detail in Section 3-3.

Current collectors also play vital roles on cell performances. For example, placing the current collector right above the anode surface results in the decrease of gas velocity around it, and thus Sherwood number. This also makes fuel species to travel longer path to three-phase-boundaries (TPB), and hence increases concentration losses. Therefore, locations of current collectors should be carefully selected to maximize the diffusion of fuel species to catalyst layers. Vogler et al. [43] placed current collectors at the edge of SOFC (far away from cell center) in their experiment work to maximize the diffusion of fuel species. In the current 2D numerical work, current collectors are placed at the interface between ceramic holders and SOFCs, while realistic wire-based current collectors can be only placed in 3D space. At the anode current collector, zero voltage and zero gradient conditions are specified for electrons and ions, respectively. At the cathode current corrector, flux boundary condition (current) and zero gradient are specified for electrons and ions, respectively.

At all walls (brown lines), zero-gradient boundary conditions are specified. Detailed boundary conditions used in this work are summarized in Supplementary material III. The physical properties, operating conditions of validation cases are listed in Tables 1 and 2, respectively. Due to lack of information in prior literature, electro-chemical properties of YSZ-based SOFCs are used for some cases and marked in the table. This may potentially cause the deviation between experimental and numerical results.

Governing equations are numerically discretized and solved by using a commercial CFD package, Fluent® (version 15.0) and the SIMPLE algorithm is used for the pressure-velocity coupling [44]. Electronic and ionic potential equations are implemented to the domain by adding customized user-defined-scalars (UDS). The source terms, constitutive relationships and boundary conditions are applied with user-defined-functions (UDF). A charge imbalance less than 0.01% is considered as the convergence criteria in this work. To accelerate the numerical speed, the ISAT tolerance of 0.001 is

Table 1 – Physical, geometrical parameters and operating conditions (a) assumed, (b) properties of YSZ-based SOFC are used due to the lack of information, (std) standard case, (ins) the case with insulation over the cathode side surface.

Quantity	Value
Properties of porous media and the ceramic holder	
Anode thickness	175 μm [7,8]
Cathode thickness	250 μm [7,8]
Electrolyte thickness	170 μm (validation) [7,8] 50 μm (case study)
Porosity of anode/cathode	0.37/0.3 [8]
Tortuosity of anode/cathode	3.5/4 [8]
Volume fraction of SDC in anode/cathode	0.38/0.5 [7]
Permeability of anode/cathode/porous burner	1.0×10^{-12} (a)/1.0×10^{-12} (a)/1.0×10^{-8} m^2 (a)
Heat conductivity of SOFC/ceramic holder	7 (a)/30 (a) W $m^{-1}K^{-1}$
Emissivity at the cathode side surface	0.8 (std)/0.4 (ins)
Heat transfer coefficient at the cathode side surface	15 (std)/7.5 (ins) W m^{-2} K^{-1}
Electronic conductivity of anode	12000 S m^{-1} [35] (b)
Electronic conductivity of cathode	30000 S m^{-1} [35] (b)
Properties of SDC	
Pre-exponential factor electronic conductivity of the SDC	4.0×10^{10} [34] S m^{-1}
Activation energy of electronic conductivity of the SDC	222.8 [34] kJ/mol
Pre-exponential factor ionic conductivity of the SDC	5.2×10^{7} [8] K^{-1}
Activation energy of ionic conductivity of the SDC	77.2 [8] kJ/mol
Electrochemistry	
Reference current density ($j_{0,i,ref}$) for H_2/CO/O_2	1.28×10^{11} [9] (b)/4.23×10^{11} [9] (b)/5.9×10^{11} [8] A m^{-3}
Activation energy for exchange current density ($E_{act,i,ex}$) for H_2/CO/O_2	45.8 [9] (b)/91.6 [9] (b)/88.6 [8] kJ/mol
Symmetric factor (α_i)	0.5 (a)

used for the first 2000 iterations and is gradually reduced to 3×10^{-5} for the better accuracy.

Results and discussions

Model validation

Before elucidating detailed multi-dimensional effects occurring in DFFCs, the present numerical model is validated against experimentally measured polarization curves for various operating conditions, such as cell-to-burner distance (d) and fuel equivalence ratio. Comparisons of numerical predictions and experiments in terms of polarization curves are presented in Fig. 2. Both numerical and experimental results show better polarization curves at higher fuel equivalence ratio (ϕ) and smaller cell-to-burner distance (d). These results indicate that the current multi-dimensional model yields the qualitative conformity with experimental results. Also, experimentally and numerically measured OCVs are in good agreement, which implies that the proposed model also captures the electronic cross-current in electrolytes well.

Table 2 – Validation cases.

Case	Distance between burner and SOFC	Equivalence Ratio
1	10 mm	1.1
2	10 mm	1.2
3	10 mm	1.3
4	20 mm	1.1
5	20 mm	1.2
6	20 mm	1.3

However, quantitative deviations exist with experimental data, especially in cases with the cell-to-burner distance of 20 mm.

These discrepancies could be mainly attributed to the over-simplified modeling for the porous-burner zone, as well as the uncertainties in the electro-chemical properties. To explain limitations of the current porous-burner model, gas velocities at the interface between the porous burner and the flow-field are first compared in Fig. 3a ($\phi = 1.3$) for cases with $d = 10$ mm and 20 mm. Both results show non-uniform gas velocities distributions at the burner and open flow-field interface, which is due to the SOFC and the ceramic holder blocking the gas flow and therefore changing pressure-fields. Especially, the case of $d = 20$ mm shows higher gas velocity at the region close to the centerline, compared to the case with $d = 10$ mm. Due to the higher gas velocity around the centerline, the flame front in the case of $d = 20$ mm is located further downstream, compared to the case with $d = 10$ mm as seen in OH distributions in Fig. 3b.

In reality, however, the flame front in the case of $d = 20$ mm is likely to be located more closer to the burner or even inside the burner, considering that using a porous burner significantly enhances laminar flame speeds [45,46], owing to the microscopic pore structures and higher effective heat diffusivity [45,46]. In the current study, the temperature of porous burner is set to be 300 K, since the experimental paper [7] mentioned that the porous burner is being cooled by liquid water, while other detailed dimensions and properties of porous burner are not known in Ref. [7]. Therefore, flames cannot exist in the porous burner in this numerical model. Therefore, the proposed model may generally over-estimate heat transfer rates from flames to SOFCs due to under-predictions of effective flame speeds, which may also lead to over-estimated cell temperatures, while experimentally

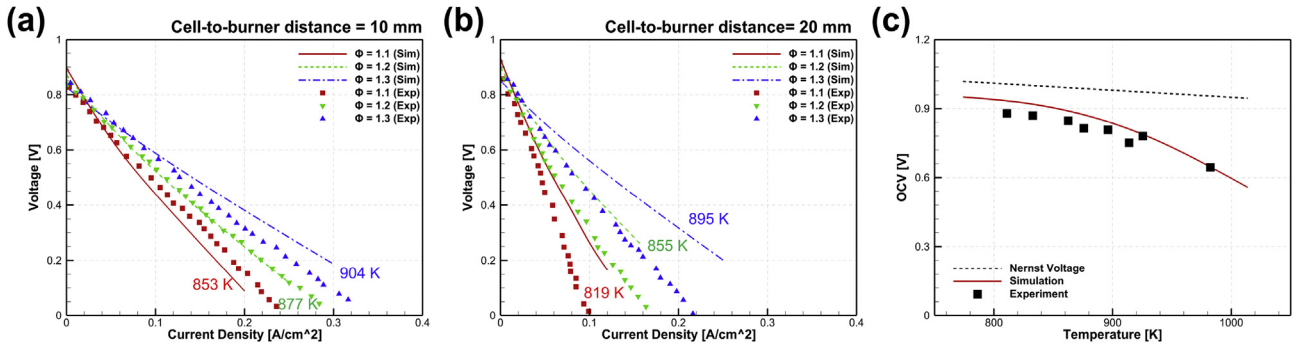

Fig. 2 – (Color Online) Comparison between experimentally [7] and numerically measured polarization curves in cases of (a) the cell-to-burner distance = 10 mm and (b) 20 mm (*numbers = numerical predictions of cell temperatures*) (c) comparison between experimentally [7,8] and numerically measured open circuit voltages (OCVs). (For interpretation of the references to colour in this figure legend, the reader is referred to the Web version of this article.)

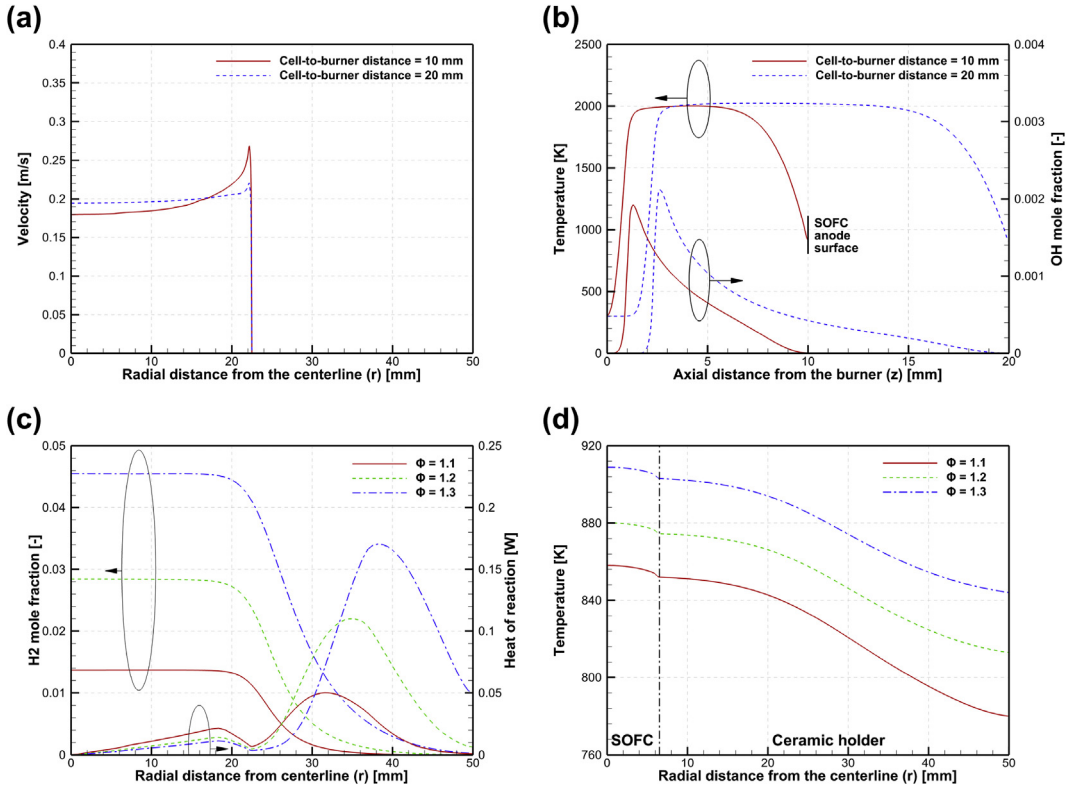

Fig. 3 – (Color Online) (a) Radial profiles of gas velocity at the interface between flow-fields and porous burners (z = 0 mm) at the condition with $\phi = 1.3$, (b) centerline profiles OH mole fractions and temperatures at the condition with $\phi = 1.3$, (c) Radial profiles of hydrogen and heat of reaction at z = 5 mm in the case with d = 10 mm at different equivalence ratios (d) Radial profiles of temperatures at solid zones (SOFCs + ceramic holders) at different equivalence ratios. (For interpretation of the references to colour in this figure legend, the reader is referred to the Web version of this article.)

measured cell temperatures are absent in Ref. [7]. This may be the main reason of over-estimated polarization curves for cases with $d = 20$ mm.

This implies that the physical processes occurring in porous burners, such as pore-scale combustion, radiation, gas pre-heating and the liquid water cooling, can be also important factors to be considered into numerical models of DFFCs, which will be discussed in future works. The work by Wang et al. [10] experimentally demonstrates that using different types of porous burner significantly affects performances of DFFCs.

The proposed model also explains why average cell temperatures increase with fuel equivalence ratio ($\phi = 1.1$–1.3). The main reason is the secondary oxidation of exhaust gas from premixed flame. Radial profiles of hydrogen and heat of reaction at $z = 5$ mm in cases of $d = 10$ mm are plotted in Fig. 3c. As fuel equivalence ratio increases, the heat of reaction due to the secondary reaction increases due to the increasing

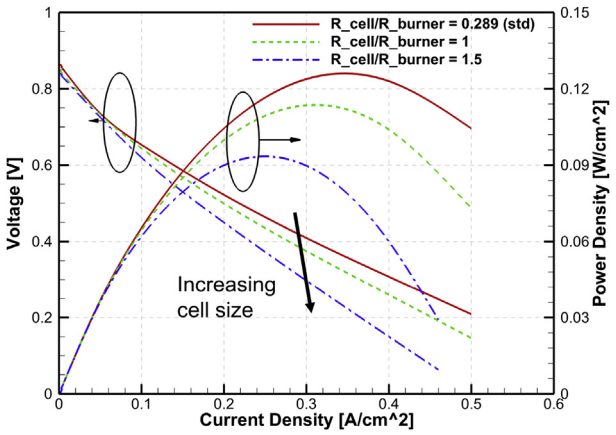

Fig. 4 – (Color online) Comparisons of numerically measured polarization curves of cells with different sizes. (For interpretation of the references to colour in this figure legend, the reader is referred to the Web version of this article.)

hydrogen concentration in the exhaust gas. This increasing fuel equivalence ratio attributes higher heat transfer rate to the ceramic holder and SOFC and higher cell temperature as seen in Fig. 3d. The effect of the secondary oxidation is a very important phenomenon to be considered and can be only captured by multi-dimensional models.

Numerical investigation of physical phenomena in DFFCs with different cell sizes

As discussed in the introduction, practical DFFCs are likely to feature larger cell sizes to achieve higher power outputs. Considering this, we select DFFCs with different sizes of SOFCs to numerically analyze potential multi-dimensional effects in real-world DFFCs. We also select DFFCs with thinner electrolyte (50 μm), compared to the DFFC by Kronemayer et al. [7], to investigate physics in high-power DFFCs. Three particular sizes of SOFCs are selected and shown below.

- R_{Cell} = 6.5 mm: baseline cell (has same size to the cell by Kronemayer et al. [7])
- R_{Cell} = 22.5 mm: a case that the cell and the burner have same radius (R_{Cell}/R_{Burner} = 1)
- R_{Cell} = 33.75 mm: a case that the cell has larger radius than the burner (R_{Cell}/R_{Burner} = 1.5)

Numerically measured polarization curves with different cell sizes are shown in Fig. 4, which shows that the cell performances become gradually worse as the cell size increases. Compared to the baseline case (0.125 W cm^{-2}), the case with R_{cell}/R_{burner} = 1.5 (0.091 W cm^{-2}) shows roughly 27% lower maximum power density.

To elucidate underlying reasons of this phenomenon, radial distributions of temperature and ionic conductivity in electrolytes in the three DFFCs are first plotted in Fig. 5. As seen in Fig. 5a, temperature is highest at the centerline and decreases along the radial direction due to heat dissipation from the cathode side surface. Due to this heat dissipation, the temperature distribution becomes more non-uniform as the radius of the cell increases (Fig. 5b). As a result, the distribution of ionic conductivity also becomes non-uniform (Fig. 5c), which influences the uniformity of the current density distribution and the overall Ohmic loss.

The distributions of fuel species in the three DFFCs operating with the current density of 0.3 A-cm^{-2} are compared in Fig. 6. As seen in Fig. 6a-c, the differences in hydrogen distributions in open flow-fields among the three cases are small. This implies that electrochemical reactions have a negligible impact on the species distributions of the exhaust gases, and most of fuel species are burned by secondary oxidation. As seen in the figures, secondary oxidation determines the region where fuel species are abundant. Therefore, secondary oxidation is an important factor to be considered when choosing a size of a SOFC. For example, the cell with R_{cell}/R_{burner} = 1.5 is suffered by low hydrogen concentration around the edge of the SOFC as seen in Fig. 6c-d, since the edge of the SOFC is very close to the secondary oxidation zone. This low fuel concentration increases over-potential and therefore decreases current density around the edge region. The effect of low fuel species concentration at the edge area will be discussed in more detail in the next section.

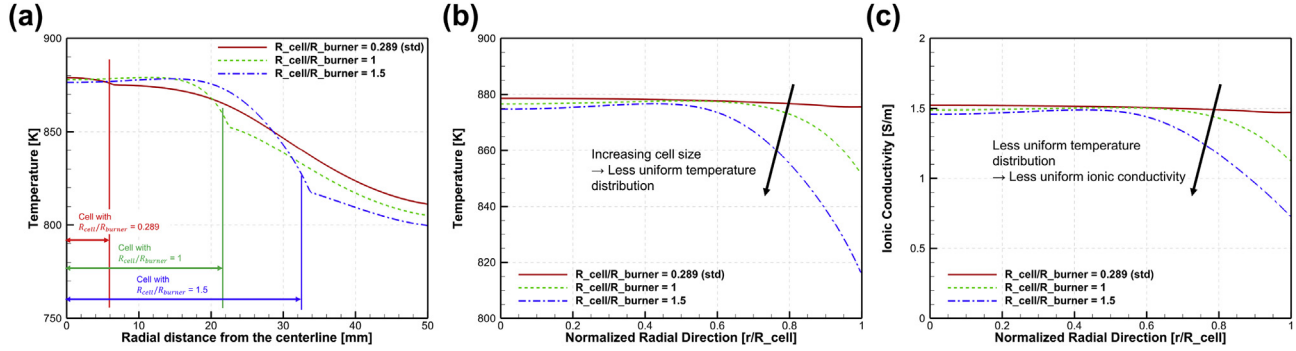

Fig. 5 – (Color online) Comparisons of (a) distributions of temperature in solid zones along the radial direction (b) distributions of temperature in electrolytes along the normalized radial direction (c) distributions of ionic conductivity in electrolytes along the normalized radial direction for the three DFFCs with different sizes of SOFCs. (For interpretation of the references to colour in this figure legend, the reader is referred to the Web version of this article.)

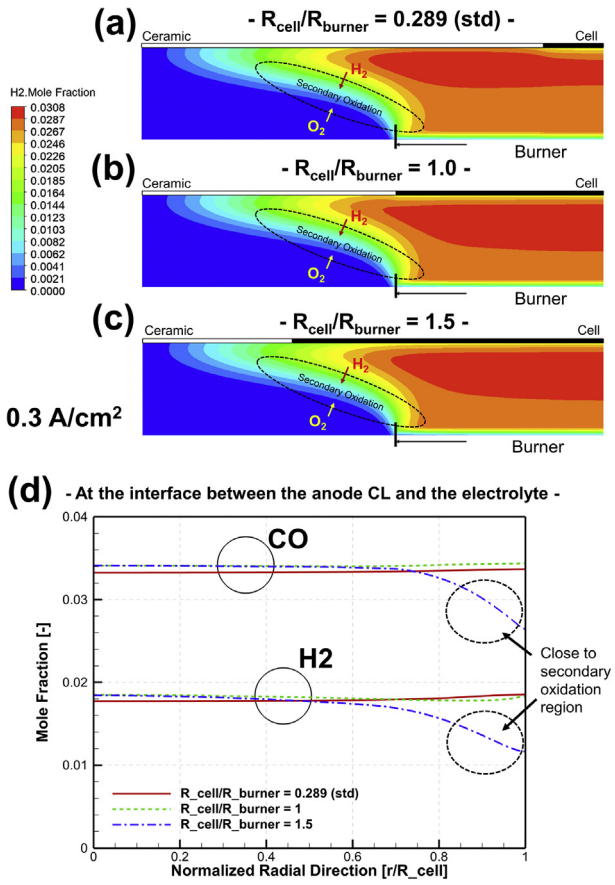

Fig. 6 – (Color online) Contours of H_2 mole fraction distributions in the open flow-fields in the case with (a) $R_{Cell}/R_{Burner} = 0.289$, (b) $R_{Cell}/R_{Burner} = 1.0$ and (c) $R_{Cell}/R_{Burner} = 1.5$ at the current density of 0.3 A cm^{-2}. (d) Comparisons of distributions of H_2 and CO at the interfaces between the anode CLs and the electrolytes along the normalized radial direction for the three DFFCs at the current density of 0.3 A cm^{-2}.

The electron transport in the electrodes is also affected by the size of SOFC, as shown in Fig. 7a. Larger SOFCs tend to generate more electrical current and have longer travel distance for electrons, resulting in more non-uniform voltage distribution and higher Ohmic loss in electrodes. Also, this non-uniform voltage distribution causes non-uniform distribution of overpotential, which causes a non-uniform current density distribution (Fig. 7b). To overcome the negative consequences from non-uniform voltage distribution, one may use a web-like wire structure for the current collector, instead of a single-wire used in the experiment for the current collector [7]. This can be helpful for decreasing Ohmic loss occurring in electrodes. However, web-like wire structure may result in worse diffusion of fuel species to TPBs, as discussed in Section 2.3.

Current density distributions (Fig. 7b) are directly influenced by the distributions of temperature (Fig. 5), species (Fig. 6) and voltage (Fig. 7a). We can see that current density distributions in DFFCs are M-shaped and become more non-uniform as the size of SOFC increases. The lower current density around the cell center is due to higher voltage around the centerline. However, the lower current density around the cell edge is originated from the consequences of lower fuel concentration and lower temperature in the area.

DFFCs operated on high temperature (~1000 K)

Commercial DFFCs may be operated on wide range of temperatures due to the growing interests of DFFCs as mobile applications. For example, DFFCs may suffer severe decrease of temperature due to strong convection over the surface at cathode side, which can decrease power density. On the other hand, the cell temperature can be increased to enhance power density. Tucker and Ying [19] recently demonstrated that adding insulations over cathode surfaces can increase power density of DFFCs. In this section, we consider the case that the heat transfer rate from the surface on the cathode side is 50% effective to numerically observe the detailed physics in DFFCs at high temperature (~1000 K). This can be realized by setting

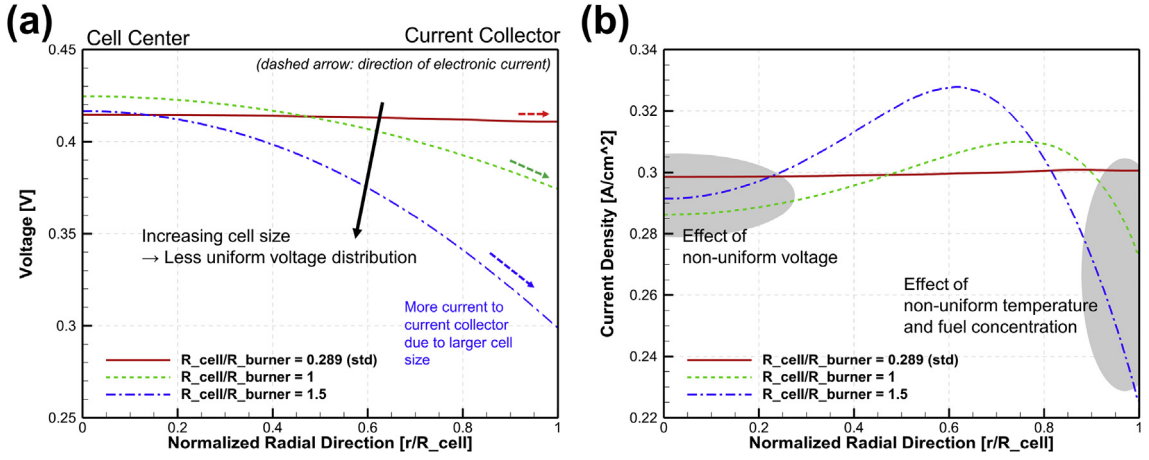

Fig. 7 – (Color online) Comparisons of (a) distributions of voltage in cathode (b) distributions of current density in electrolytes along the normalized radial direction for the three DFFCs with different sizes of SOFCs. (For interpretation of the references to colour in this figure legend, the reader is referred to the Web version of this article.)

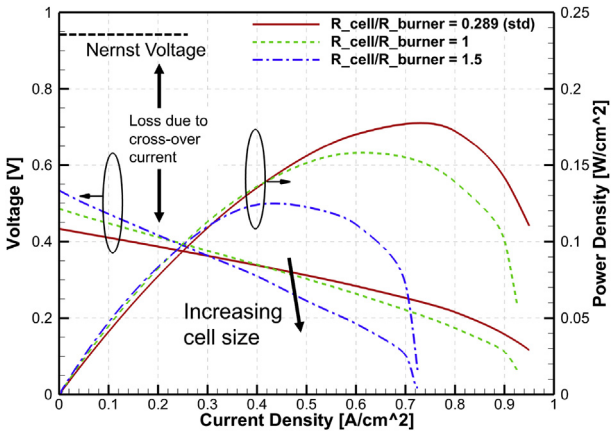

Fig. 8 – (Color online) *(insulation over the cathode side surface)* Comparisons of numerically measured polarization curves of cells with different sizes. (For interpretation of the references to colour in this figure legend, the reader is referred to the Web version of this article.)

the emissivity and heat transfer coefficient to be 50%, compared to the baseline condition.

Polarization curves of the three DFFCs under the high temperature condition are compared in Fig. 8. Similar to the standard case (Fig. 4), the case with $R_{cell}/R_{burner} = 1.5$ (0.120 W cm^{-2}) shows roughly 31% lower maximum power density, compared to the baseline cell (0.176 W cm^{-2}). However, compared to the polarization curves under the standard condition (Fig. 4), there are two major differences to point out. First, much lower OCVs are present due to higher electronic conductivity of SDC electrolytes caused by higher operating temperature. Numerically measured OCVs are 0.4–0.5 V lower, compared to Nernst voltages (at 1020 K). Second, DFFCs suffer from large concentration loss at high current density and the limiting current density decreases with increasing sizes of SOFCs.

Mole fraction profiles of H_2 (Fig. 9a) and CO (Fig. 9b) at the anode/electrolyte interface at different current densities are plotted to elucidate the underlying mechanisms of large concentration loss in the DFFC with a large SOFC (the case with $R_{cell}/R_{burner} = 1.5$). It is seen that overall H_2 and CO molar concentrations at the anode/electrolyte interface decrease with current density. The interesting thing is that fuel species approach zero starting from the edge of the SOFC, which is mainly attributed from the fact that the edge of SOFC is very close to the secondary oxidation zone as discussed in Fig. 6. At 0.7 A cm^{-2}, H_2 concentration at the edge area is very close to zero and the edge area relies on CO for the electrochemical reaction. At 0.725 A cm^{-2}, however, the edge area also suffers from CO starvation, which attributes to the rapid decrease of cell voltage shown in Fig. 8.

Ionic current density distributions in electrolyte (Fig. 10a) are plotted to observe the effect of fuel starvation around 0.7 A cm^{-2} on ionic current density distributions. From 0 A cm^{-2} to 0.7 A cm^{-2}, the ionic current density increases at all region of SOFCs. However, owing to the H_2 and CO starvation around 0.7 A cm^{-2}, the current density around the edge area start to quickly decrease as marked by blue circle. This effect decreases the effective area for the electrochemical reactions and makes the ionic current density concentrated to the center area, which consequently increases the overpotential and Ohimic losses around the center area.

Electronic cross-over current distributions in SDC electrolyte in the DFFC with a large SOFC (the case with $R_{cell}/R_{burner} = 1.5$) are presented in Fig. 10b. At 0 A cm^{-2}, the electronic cross-over current is locally as high as 0.7 A cm^{-2}, and therefore very significant (averaged electronic current density = 0.47 A cm^{-2}). This results in the decrease of OCVs and low fuel cell efficiencies exist under low current density operations. The electronic cross-over current density decreases with total current density owing to the decrease of cell voltage. However,

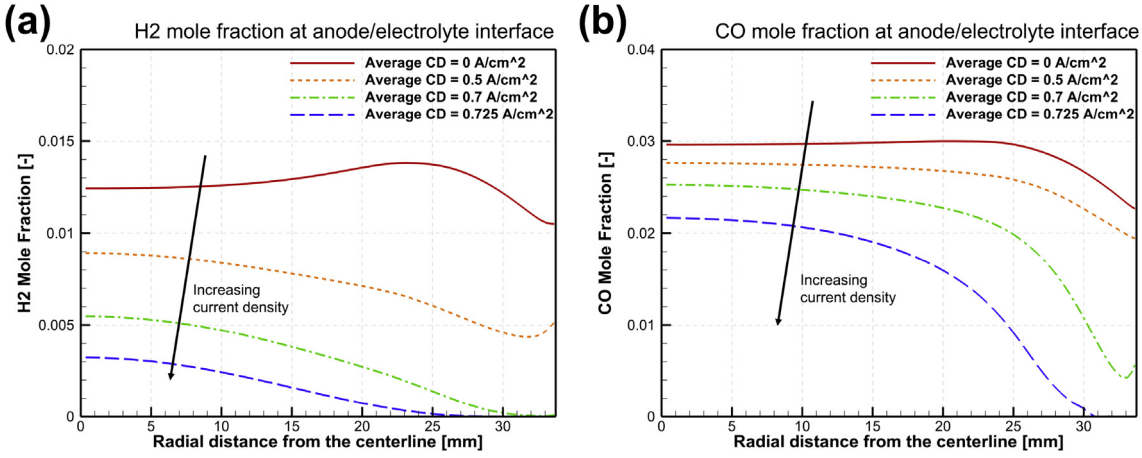

Fig. 9 – (Color online) *(insulation over the cathode side surface)* Comparisons of distributions of (a) H2 mole fraction and (b) CO mole fraction at the interface between the anode and the electrolyte at different average current densities. The DFFC with $R_{Cell}/R_{Burner} = 1.5$ is selected in this figure to emphasize the effect of non-uniform fuel species distributions on cell performances. (For interpretation of the references to colour in this figure legend, the reader is referred to the Web version of this article.)

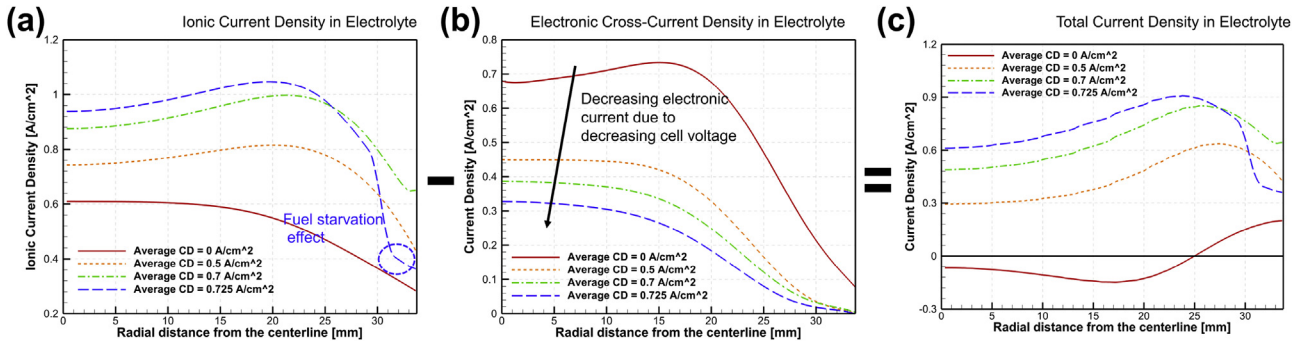

Fig. 10 – (Color online) *(insulation over the cathode side surface)* Comparisons of distributions of (a) ionic current density (b) electronic cross-current density and (c) total current density in the electrolyte at different average current densities. The DFFC with $R_{Cell}/R_{Burner} = 1.5$ is selected in this figure to emphasize the effect of non-uniform fuel species distributions on cell performances. (For interpretation of the references to colour in this figure legend, the reader is referred to the Web version of this article.)

it is still very high as 0.3 A cm^{-2} around the cell center, resulting in large amount of electro-chemically generated current being wasted.

Fig. 10c shows total current density distributions in SDC electrolyte in the DFFC with a large SOFC (the case with $R_{cell}/R_{burner} = 1.5$). As seen in the figure, there is a significant current loss around the cell center. Comparing with the ionic current density distributions, the total current distributions around the cell center is 0.3–0.7 A cm^{-2} lower depending on the average current density. At current density around 0.7 A cm^{-2}, the cell suffers from fuel starvation around the edge area as discussed previously.

Numerical results from this work points out two important barriers to be overcome for the future development of DFFCs. First is the large electronic cross-over current at high temperature operation. To overcome this, one may use different electrolyte structures and materials, such as using yttria-stabilized zirconia (YSZ) as an electrolyte or bi-layer structured electrolyte. In particular, bi-layer structured electrolytes have shown great ionic conductivity at low operating temperature (700–900 K) and low electronic conductivity at high temperature (>950 K) [12,13,32,34], and therefore are good candidates for DFFCs as they are subjected to wide range of temperature variations for mobile applications. However, widespread adoption of bi-layer structured electrolytes still requires deep understanding of physics occurring at the two heterogeneous layers.

Second is the severe concentration loss around the edge area of SOFCs. It is possible to alleviate this concentration loss by using a different flow-structure to place secondary oxidation zone much farther from SOFCs. For example, one can place a diverging channel around the burner to prevent the secondary oxidation to increase fuel species concentration at the edge area. The effect of using different flow structures on cell performances can be studied by experimental approaches and current numerical model. The detailed discussions on the effect of using different flow structures will be presented in future works, since the major focus is placed on the illustration of physical phenomena associated with multi-dimensional effects.

Conclusion

In this study, a two-dimensional model has been developed to numerically investigate the multi-dimensional effects occurring in DFFCs at various conditions. Numerical results obtained by the 2D model show good agreement with experiments by Kronemayer et al. [7]. The limitations of the proposed model are also identified to illustrate the uncaptured physical phenomena induced from the microstructure of the porous burner in the DFFC.

The proposed model shows that the power density of a DFFC is noticeably reduced by increasing the size of the SOFC due to the increasing multi-dimensional effects. At the edge region of the SOFC, temperature and fuel species concentrations tend to be lower than around the center region. The lower temperature at the edge area is due to the heat dissipation from the SOFC, and the lower fuel concentration at the edge area is because the edge area is closer to the secondary oxidation zone. At the center region of SOFCs, the voltage tends to be the highest, which causes lower over-potential and hence lower current density. Therefore, the current density distributions in DFFCs are likely to have an M-type shape, according to the proposed numerical model.

At higher operating temperatures (~1000 K), electronic cross-over currents and non-uniform fuel species distribution play more significant roles on cell performance. It is found that electronic cross-over current in SDC electrolyte in DFFCs at ~1000 K can be up to 0.5 A cm^{-2}, which attributes significant voltage loss. Also, lower fuel species distributions at the edge area limit the current density of DFFCs, as fuel starvation is likely to occur at the edge area of the SOFC. Overall, the DFFC with a large SOFC (R=33.75 mm) has 30% lower power density than the DFFC with a small SOFC (R=6.5 mm), owing to aforementioned effects.

In summary, non-uniform distributions of temperature, fuel species, voltage and electronic cross-over current are found to be the main factors to be considered for the development of commercial DFFCs. Discussions are made to prevent the cell performance losses due to above multi-

dimensional effects. Efforts are ongoing to pave a way to improve the performance of DFFCs by using the current numerical model, which are able to analyze the impact of those four factors.

Appendix. Derivation of the effective oxygen partial pressure in SDC electrolytes

We first assume negligible temperature variations along thickness direction, while the temperature can still vary along the other directions. By introducing a non-dimensionalized thickness $\bar{z} = (z - z_{an|el})/L_{el}$, Eq. (18) can be re-written as:

$$P_{O_2}(x)^{-0.25} = A_0 + \left(P_{O_2}(x_{an|el})^{-0.25} - A_0\right)\exp\left(\frac{-\eta_{Ohm}F}{RT}\bar{z}\right) \quad (A1)$$

For convenience, we introduce new variables, such as $a_0 = A_0$, $a_1 = P_{O_2}(x_{an|el})^{-0.25} - A_0$ and $a_3 = (-\eta_{Ohm}F)/(RT)$. Then, the RHS of Eq. (22) can be expressed as:

$$\int_{\bar{z}=0}^{\bar{z}=1} d\bar{z}\Big/\left(P_{O_2}(\bar{z})^{-0.25}\right) = \int_{\bar{z}=0}^{\bar{z}=1} d\bar{z}/(a_0 + a_1\exp(a_2\bar{z})) \quad (A2)$$

For further simplifications, we define a variable such that $z^* = a_1\exp(a_2\bar{z})$. Since a_1 and a_2 have no variations along thickness direction, the $d\bar{z}$ can be re-expressed as $d\bar{z} = dz^*/(a_2 z^*)$. Then, the RHS of Eq. (A2) can be re-written as:

$$\int_{z^*=a_0+a_1}^{z^*=a_0+a_1\exp(a_2)} dz^*/(a_2(a_0 + z^*)z^*) \quad (A3)$$

The integration of Eq. (A3) is quite simple. After the integration of Eq. (A3), the effective oxygen partial pressure in SDC electrolytes can be given as

$$P_{O_2,eff} = \left(\frac{1}{a_0 a_2}\left(\ln\frac{a_1\exp a_2}{a_0 + a_1\exp a_2} + \ln\frac{a_1}{a_0 + a_1}\right)\right)^{-4} \quad (A4)$$

Appendix A. Supplementary data

Supplementary data to this article can be found online at https://doi.org/10.1016/j.ijhydene.2018.12.169.

REFERENCES

[1] Wang K, Ran R, Hao Y, Shao Z, Jin W, Xu N. A high-performance no-chamber fuel cell operated on ethanol flame. J Power Sources 2008;177:33–9. https://doi.org/10.1016/j.jpowsour.2007.11.004.

[2] Zhu X, Wei B, Lü Z, Yang L, Huang X, Zhang Y, Liu M. A direct flame solid oxide fuel cell for potential combined heat and power generation. Int J Hydrogen Energy 2012;37:8621–9. https://doi.org/10.1016/j.ijhydene.2012.02.161.

[3] Wang Y, Shi Y, Ni M, Cai N. A micro tri-generation system based on direct flame fuel cells for residential applications. Int J Hydrogen Energy 2014;39:5996–6005. https://doi.org/10.1016/j.ijhydene.2014.01.183.

[4] Wang K, Zeng P, Ahn J. High performance direct flame fuel cell using a propane flame. Proc Combust Inst 2011;33:3431–7. https://doi.org/10.1016/j.proci.2010.07.047.

[5] Sun L, Hao Y, Zhang C, Ran R, Shao Z. Coking-free direct-methanol-flame fuel cell with traditional nickel-cermet anode. Int J Hydrogen Energy 2010;35:7971–81. https://doi.org/10.1016/j.ijhydene.2010.05.048.

[6] Milcarek RJ, Ahn J. Rich-burn, flame-assisted fuel cell, quick-mix, lean-burn (RFQL) combustor and power generation. J Power Sources 2018;381:18–25. https://doi.org/10.1016/j.jpowsour.2018.02.006.

[7] Kronemayer H, Barzan D, Horiuchi M, Suganuma S, Tokutake Y, Schulz C, Bessler WG. A direct-flame solid oxide fuel cell (DFFC) operated on methane, propane, and butane. J Power Sources 2007;166:120–6. https://doi.org/10.1016/j.jpowsour.2006.12.074.

[8] Vogler M, Horiuchi M, Bessler WG. Modeling, simulation and optimization of a no-chamber solid oxide fuel cell operated with a flat-flame burner. J Power Sources 2010;195:7067–77. https://doi.org/10.1016/j.jpowsour.2010.04.030.

[9] Tucker MC. Personal power using metal-supported solid oxide fuel cells operated in a camping stove flame. Int J Hydrogen Energy 2018;43:8991–8. https://doi.org/10.1016/j.ijhydene.2018.03.161.

[10] Wang Y, Zeng H, Shi Y, Cao T, Cai N, Ye X, Wang S. Power and heat co-generation by micro-tubular flame fuel cell on a porous media burner. Energy 2016;109:117–23. https://doi.org/10.1016/j.energy.2016.04.095.

[11] Milcarek RJ, Garrett MJ, Ahn J. Micro-tubular flame-assisted fuel cell stacks. Int J Hydrogen Energy 2016;41:21489–96. https://doi.org/10.1016/j.ijhydene.2016.09.005.

[12] Hirasawa T, Kato S. A study on energy conversion efficiency of direct flame fuel cell supported by clustered diffusion microflames. J Phys Conf Ser 2014;557. https://doi.org/10.1088/1742-6596/557/1/012120.

[13] Wang K, Milcarek RJ, Zeng P, Ahn J. Flame-assisted fuel cells running methane. Int J Hydrogen Energy 2015;40:4659–65. https://doi.org/10.1016/j.ijhydene.2015.01.128.

[14] Bao C, Jiang Z, Zhang X. Mathematical modeling of synthesis gas fueled electrochemistry and transport including H_2/CO co-oxidation and surface diffusion in solid oxide fuel cell. J Power Sources 2015;294:317–32. https://doi.org/10.1016/j.jpowsour.2015.06.070.

[15] Ideris A, Croiset E, Pritzker M. Ni-samaria-doped ceria (Ni-SDC) anode-supported solid oxide fuel cell (SOFC) operating with CO. Int J Hydrogen Energy 2017;42:9180–7. https://doi.org/10.1016/j.ijhydene.2016.05.203.

[16] Shri Prakash B, Pavitra R, Senthil Kumar S, Aruna ST. Electrolyte bi-layering strategy to improve the performance of an intermediate temperature solid oxide fuel cell: a review. J Power Sources 2018;381:136–55. https://doi.org/10.1016/j.jpowsour.2018.02.003.

[17] Ahn JS, Pergolesi D, Camaratta MA, Yoon H, Lee BW, Lee KT, Jung DW, Traversa E, Wachsman ED. High-performance bilayered electrolyte intermediate temperature solid oxide fuel cells, Electrochem. Commun Now 2009;11:1504–7. https://doi.org/10.1016/j.elecom.2009.05.041.

[18] Ishihara T, Eto H, Yan J. Intermediate temperature solid oxide fuel cells using LaGaO3based oxide film deposited by PLD method. Int J Hydrogen Energy 2011;36:1862–7. https://doi.org/10.1016/j.ijhydene.2009.12.174.

[19] Tucker MC, Ying AS. Metal-supported solid oxide fuel cells operated in direct-flame configuration. Int J Hydrogen Energy 2017;42:24426–34. https://doi.org/10.1016/j.ijhydene.2017.07.224.

[20] Wang Y, Zeng H, Shi Y, Cao T, Cai N. Mathematical modeling of a porous media burner based methane flame fuel cell. J Electrochem Soc 2017;164:E3627–34. https://doi.org/10.1149/2.0651711jes.

[21] Kakaç S, Pramuanjaroenkij A, Zhou XY. A review of numerical modeling of solid oxide fuel cells. Int J Hydrogen

Energy 2007;32:761–86. https://doi.org/10.1016/j.ijhydene.2006.11.028.
[22] Burali N, Lapointe S, Bobbitt B, Blanquart G, Xuan Y. Assessment of the constant non-unity Lewis number assumption in chemically-reacting flows, Combust. Theory Mod 2016;20:632–57. https://doi.org/10.1080/13647830.2016.1164344.
[23] Frenklach VLM, Wang H, Goldenberg M, Smith GP, Golden DM, Bowman CT, Hanson RK, Gardiner WC. GRI-Mech—An optimized detailed chemical reaction mechanism for methane combustion. 1995.
[24] V.L. M. Frenklach, H. Wang, C.-L. Yu, M. Goldenberg, C.T. Bowman, R.K. Hanson, D.F. Davidson, E.J. Chang, G.P. Smith, D.M. Golden, W.C. Gardiner, No Title, (n.d.). http://www.me.berkeley.edu/gri_mech/.
[25] Pope SB. Computationally efficient implementation of combustion chemistry using in situ adaptive tabulation. Combust Theor Model 1997;1:41–63. https://doi.org/10.1088/1364-7830/1/1/006.
[26] Kumar A, Mazumder S. Assessment of various diffusion models for the prediction of heterogeneous combustion in monolith tubes. Comput Chem Eng 2008;32:1482–93. https://doi.org/10.1016/j.compchemeng.2007.06.024.
[27] Xuan Y, Blanquart G. Numerical modeling of sooting tendencies in a laminar co-flow diffusion flame. Combust Flame 2013;160:1657–66. https://doi.org/10.1016/j.combustflame.2013.03.034.
[28] Bird RB, Stewart WE, Lightfoot EN. Transport phenomena. 1960.
[29] Menon SK, Boettcher PA, Ventura B, Blanquart G. Hot surface ignition of n-hexane in air. Combust Flame 2016;163:42–53. https://doi.org/10.1016/j.combustflame.2015.08.011.
[30] C.H. Bosanquet, British TA report BR-507, n.d.
[31] Howell JR, Menguc MP, Siegel R. Thermal radiation heat transfer. CRC press; 2010.
[32] Cheng P. Two-dimensional radiating gas flow by a moment method. AIAA J 1964;2:1662–4. https://doi.org/10.2514/3.2645.
[33] Hottel HC, Sarofim AF. Radiative transfer. New York: McGraw-Hill; 1967.
[34] Smith TF, Shen ZF, Friedman JN. Evaluation of coefficients for the weighted sum of gray gases model. J Heat Tran 1982;104:602. https://doi.org/10.1115/1.3245174.
[35] Andersson M, Yuan J, Sundén B. SOFC modeling considering hydrogen and carbon monoxide as electrochemical reactants. J Power Sources 2013;232:42–54. https://doi.org/10.1016/j.jpowsour.2012.12.122.
[36] Shen S, Yang Y, Guo L, Liu H. A polarization model for a solid oxide fuel cell with a mixed ionic and electronic conductor as electrolyte. J Power Sources 2014;256:43–51. https://doi.org/10.1016/j.jpowsour.2014.01.041.
[37] Zhang X, Robertson M, Deĉes-Petit C, Qu W, Kesler O, Maric R, Ghosh D. Internal shorting and fuel loss of a low temperature solid oxide fuel cell with SDC electrolyte. J Power Sources 2007;164:668–77. https://doi.org/10.1016/j.jpowsour.2006.10.087.
[38] Shen S, Guo L, Liu H. A polarization model for solid oxide fuel cells with a Bi-layer electrolyte. Int J Hydrogen Energy 2016;41:3646–54. https://doi.org/10.1016/j.ijhydene.2015.12.162.
[39] Yuan U, Shi, Pal. Analytic solution for charge transport and chemical-potential variation in single-layer and multilayer devices of different mixed-conducting oxides. J Electrochem Soc 1996;143:3214. https://doi.org/10.1149/1.1837189.
[40] Shen S, Guo L, Liu H. An analytical model for solid oxide fuel cells with bi-layer electrolyte. Int J Hydrogen Energy 2013;38:1967–75. https://doi.org/10.1016/j.ijhydene.2012.11.084.
[41] Gödickemeier M. Engineering of solid oxide fuel cells with ceria-based electrolytes. J Electrochem Soc 1998;145:414. https://doi.org/10.1149/1.1838279.
[42] White FM. Fluid mechanics. 8th ed. McGraw-Hill; 2015.
[43] Vogler M, Barzan D, Kronemayer H, Schulz C, Horiuchi M, Suganuma S, Tokutake Y, Warnatz J, Bessler WG. Direct-flame solid-oxide fuel cell (DFFC): a thermally self-sustained, air self- breathing, hydrocarbon-operated SOFC system in a simple, No-chamber setup. ECS Trans 2007;7:555–64. https://doi.org/10.1149/1.2729136.
[44] Patankar SV. Numerical heat transfer and fluid flow. New York: Hemisphere Publishing Corp.; 1980.
[45] Khanna V, Goel R, Ellzey JL. Measurements of emissions and radiation for methane combustion within a porous medium burner. Combust Sci Technol 1994;99:133–42. https://doi.org/10.1080/00102209408935429.
[46] Hsu P-F, Evans WD, Howell JR. Experimental and numerical study of premixed combustion within nonhomogeneous porous ceramics. Combust Sci Technol 1993;90:149–72. https://doi.org/10.1080/00102209308907608.

List of Symbols

A: Pre-exponential factors
c_p: Heat capacity
D_h: Hydraulic diameter (m)
D_{i-j}: Binary diffusivity of species i to j ($m^2\ s^{-1}$)
I: Current density (A cm^{-2})
j: Volumetric current density (A m^{-3})
$\overrightarrow{J}_i$: Diffusional Flux (kg m^2s)
MW: Molecular weight (kg mol^{-1})
P: Pressure (Pa)
S: Source term in transport equations
T: Temperature (K)
$\overrightarrow{u}$: Velocity (m s^{-1})
X: Mole fraction
Y: Mass fraction

Greek

ε: Porosity, Emissivity
σ_{SB}: Stefan-Boltzmann Constant (5.67×10^{-8} W m^{-2} K^{-4})
μ: Dynamic viscosity (kg $m^{-1}s^{-1}$)
ν: Kinematic viscosity ($m^2\ s^{-1}$)
τ: Tortuosity
$\overrightarrow{\tau}$: Viscous stress (Pa $m^{-1}s^{-1}$)
ρ: Density (kg m^{-3})
Φ_e: Ionic potential (V)
Φ_s: Electronic potential (V)

Superscript and Subscripts

an|el: Interface between anode and electrolyte
char: Charged object such as ion and electron
el: Electrolyte
elec: Electron
eff: Effective
el|ca: Interface between electrolyte and cathode
g: Gas
i: Species
ion: Ion